Journal of Materials Science: Materials in Electronics (2019) 30:9520–9530
https://doi.org/10.1007/s10854-019-01284-2

Impact of ZnO addition on structural, morphological, optical, dielectric and electrical performances of $BaTiO_3$ ceramics

Y. Slimani[1] · A. Selmi[2] · E. Hannachi[3] · M. A. Almessiere[1,4] · A. Baykal[5] · I. Ercan[1]

Received: 11 March 2019 / Accepted: 3 April 2019 / Published online: 6 April 2019

Abstract
$BaTiO_3/(ZnO)_x$ ceramics (x = 0, 2, 5 and 10 wt%) were produced via solid state reaction by using high energy ball milling. The morphological, structural, spectral, optical, electrical and dielectric properties were systematically investigated. X-ray diffraction indicated that all ceramics crystallize in the tetragonal structure. The grains size increases with ZnO additions. The optical band gap energy (E_g) was also evaluated and found to reduce with increasing ZnO concentration. The dielectric and electric properties revealed that an optimal ZnO content lead to obtain ceramic with high dielectric constant and low tangent loss, which are encouraging for radio frequencies and microwaves applications.

1 Introduction

The spinel structure is adopted by various materials, including catalysts, superconductors, magnetic materials, semiconductors and microwave dielectric ceramics at millimeter region [1, 2]. They are promising candidates for millimeter-wave region application. It is required to possess low dielectric constant, high quality factor and near zero temperature coefficient. Furthermore, the perovskite metal oxides with ABO_3 structure have received a great attention due to their ferroelectric, dielectric, photoelectric, pyroelectric, piezoelectric, and catalytic responses [3, 4]. These properties lead them to be invested in several technological applications such as electronics, electro-mechanical and electro-optical applications. Barium titanate $BaTiO_3$ (BTO for brevity) exhibits important dielectric constant and resistivity and low dielectric loss. It has a tetragonal ferroelectric structure at room temperature (RT) with lattice parameters a = 3.994 Å and c = 4.034 Å [5]. Numerous electronic devices are based on the use of BTO ceramics such as capacitors, passive memory storage devices, thermistors, piezoelectric transducers, sensors and many electro-optical devices [6, 7]. Several routes including hydrothermal method, sol–gel process, solid-state reaction method, chemical coprecipitation, etc. have been used to synthesize BTO ceramics with nanoscale size [8].

Many researchers over wide the world seek to improve the dielectric and electrical properties of BTO ceramics. To achieve this objective, a control of the microstructure is required. The dielectric properties could be altered by adding dopants. Various kinds of additives have been used and greatly affected the dielectric properties of perovskites ceramics. For instance, Paunović et al. [9] investigated the impacts of rare-earth (RE = Dy, Sm and La) additions on the microstructural and dielectric properties of BTO ceramics produced by the solid-state reaction. An improvement of dielectric permittivity as well as a reduction of dissipation factor was obtained for low doping additive. $BaTiO_3$–TiO_2 nanosized ceramics were produced

✉ Y. Slimani
yaslimani@iau.edu.sa; slimaniyassine18@gmail.com

✉ E. Hannachi
hannechi.essia@gmail.com

1 Department of Physics Research, Institute for Research & Medical Consultations (IRMC), Imam Abdulrahman Bin Faisal University, P.O. Box 1982, Dammam 31441, Saudi Arabia

2 Laboratoire Matériaux Organisation et Propriétés (LMOP), Université de Tunis El Manar, Campus Universitaire, 2092 El Manar, Tunisia

3 Laboratory of Physics of Materials - Structures and Properties, Department of Physics, Faculty of Sciences of Bizerte, University of Carthage, Zarzouna 7021, Tunisia

4 Department of Physics, College of Science, Imam Abdulrahman Bin Faisal University, P.O. Box 1982, Dammam 31441, Saudi Arabia

5 Department of Nano-Medicine Research, Institute for Research & Medical Consultations (IRMC), Imam Abdulrahman Bin Faisal University, P.O. Box 1982, Dammam 31441, Saudi Arabia

by several researchers with the purpose be used for dye-sensitized solar cell applications [10, 11]. The different findings showed that the $BaTiO_3$–TiO_2 nanosized ceramics could be potential for photocatalytic activity and photovoltaic systems. Zhang et al. [12] have explored the influence of SiO_2 doping on the microstructural and dielectric properties of BTO product produced by microwave sintering method. It is found that such content of SiO_2 added to BTO ceramics lead to improve the dielectric properties, particularly the permittivity increased and the dielectric loss decreased. Numerous other doping in BTO ceramics were reported in previous studies, such as NiO [13], MgO [14], CaO [15] and Y_2O_3 [16] doped $BaTiO_3$. It is showed that NiO additions reduces the relative permittivity and temperature sensitivity of the doped BTO ceramics.

ZnO is an n-type semiconductig with a wide band gap (3.2 eV) and large exciron binding energy. This makes it promising for catalytic applications. Recently, some reports focused on V_2O_5-ZnO nanocomposites and evaluated their performances on photocatalytic application [17]. Al-syadi et al. [18] prepared $(80-x)V_2O_5/20Bi_2O_3/xBaTiO_3$ composites and studied their dielctric properties. On the other hand, with low melting point and high ionic polarizability, ZnO is an important additive in dielectric ceramics, which can be utilized to improve densification and electrical properties [19]. As a prominent additive, ZnO has been broadly utilized to engineer highly efficient ceramic capacitors. A plenty of investigations revealed that ZnO has an impact on the dielectric characteristics, the sintering behavior and the microstructural improvement of perovskite ceramics [20–22]. Recently, researchers have found that the composite formed by $ZnNb_2O_6$ was very effective to enhance the densification [20]. Zn and Nb co-doped BTO ceramics prepared by microwave sintering was not only useful to enhance the densification, but also helpful to decrease the dielectric loss. Iqbal and Jamal [23] were investigated the phase and microstructure of $Ba_{1-2x}Ta_{2x}Ti_{1-x}Zn_xO_3$ ($0.005 \le x \le 0.1$). They found that the dielectric constant decreased with an increase in the dopant concentration due to second phase formation. As well, ZnO is helpful in controlling grain growth and it improves densification during sintering process [22]. Caballero et al. [24] reported the effect of ZnO added to $BaTiO_3$ on the sintering and microstructure development. They found that ZnO is helpful for grains growth of BTO ceramics. Therefore, owing to its effectiveness in controlling grain growth, ZnO appears to be an attractive additive for BTO dielectrics. With this potential in mind, we propose in this work to investigate deeply the effect of various ZnO contents inclusion on the structure, morphology, spectral, optical and dielectric properties of BTO-based products. Series of $BaTiO_3/(ZnO)_x$ ceramics, with x = 0, 2, 5 and 10 wt%, were synthesized via solid state reaction.

2 Experimental

Raw material powders of $BaCO_3$, TiO_2 and ZnO with high purity 99.99% were purchased from Sigma Aldrich company. Series of $BaTiO_3/(ZnO)_x$ ceramics, where x = 0, 2, 5 and 10 wt% were produced via solid state reaction by using planetary high energy ball milling (HEBM; Ball Mill PM 200 from Retsch). The different powders were mixed stoichiometrically in accordance to the designed compositions in ethanol. After, the mixtures were ball-milled in the planetary HEBM as a grinding media for 12 h. After drying, the grinded powders were pressed into discs with 13 mm in diameter. The obtained pellets were calcined at 1100 °C for 12 h. The steps of ball-milling, pressing into discs and calcination were repeated twice in order to achieve the desired nano-sized ceramics.

The phase identification was examined by X-ray powder diffraction (XRD; Rigaku Benchtop Miniflex) using Cu-kα radiation. The morphology was investigated by scanning electron microscope (SEM; FEI Quanta FEG). Fourier transform-infrared (FT-IR) spectra were collected using Bruker alpha-II FT-IR spectrometer in wavenumbers of 4000–400 cm^{-1}. The diffuse reflectance spectra (DRS) were registered using UV–Vis spectrophotometer (JASCO V-780). The electrical and dielectric measurements were done by using Novocontrol Technologies (Alpha-N high-resolution analyzer).

3 Results and discussion

3.1 Structural analysis

XRD patterns for various $BaTiO_3/(ZnO)_x$ ceramics with x = 0–10 wt% are presented in Fig. 1. The different XRD patterns were refined through Rietveld method by using Match! program. The Rietveld method was successfully applied to determine quantitatively phase abundances of the different crystallographic phases in the compound, as well as the lattice parameters. Typical examples of XRD refinements for ceramics with x = 0 and 5 wt% are illustrated in Fig. 2. The Bragg R_B factor and the goodness of fit χ^2 were used as the numerical criteria of fitting. The deduced phase fractions and lattice parameters are summarized in Table 1. All the XRD patterns implied that the various produced ceramics crystallized in tetragonal structure (space group *P4mm*) according to the ICCD No. 96-210-0860. It is obvious that the lattice parameters a and b decrease with increasing ZnO doping concentration in the prepared ceramics. In the current study, the development of tetragonal structure for all ceramics is

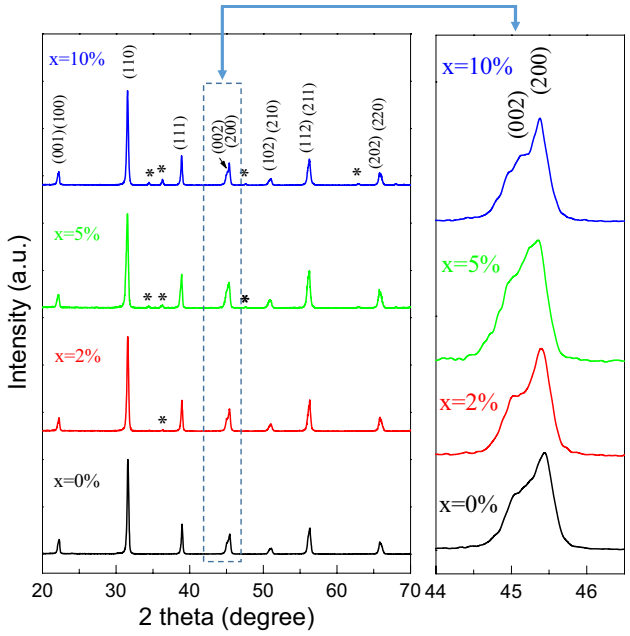

Fig. 1 XRD patterns of various synthesized $BaTiO_3/(ZnO)_x$ nanocomposites

approved by the splitting peaks of (200)/(002) reflections (inset of Fig. 1) [25]. The overlapping of these reflections and the disappearance of (200) peak are an indication to a transition from tetragonal to cubic structure. In our case, the tetragonality was maintained for different synthesized $BaTiO_3/(ZnO)_x$ ceramics with various doping levels. Furthermore, the values of c/a ratio are practically constant, indicating the preserving of tetragonality structure. It is also visible from the Fig. 1 that no impurity was found for pristine BTO sample. However, additional peaks that are corresponding to the ZnO phase (ICCD No. 96-152-7205) are identified. The concentration of secondary ZnO phase increases gradually with increasing the 'x' doping content.

The average crystallites size (D_{XRD}) is estimated for all synthesized nanocomposites by using Scherrer equation:

$$D_{XRD} = \frac{k\lambda}{\beta \cos\theta} \tag{1}$$

where k = 0.94 is a constant, $\lambda = 1.5418$ Å for Cu-Kα radiations, β is full width at half maximum, θ is Bragg's angle. The estimated D_{XRD} values for various $BaTiO_3/(ZnO)_x$ ceramics are listed in the Table 1 and are found to be in the range of 51.99–69.36 nm. Lather et al. [26] reported that when the grains size reduces, the tetragonality of the products diminishes as (c/a-1) < 1% and achieve a pseudo-cubic structure with c/a ~ 1. Compared to pristine BTO product, it is obvious that the calculated D_{XRD} increased with ZnO doping confirming the maintaining of the tetragonality.

3.2 FT-IR examination

FT-IR spectra of the prepared $BaTiO_3/(ZnO)_x$ ceramics are showed in Fig. 3. All the products revealed characteristic band at about 498 cm^{-1} that is associated to Ti–O vibration [27]. Another characteristic band with very small intensity is observed around 1450 cm^{-1} for all composites, which is mostly attributed to the signals of the Ba–Ti–O vibration [27]. No such change is noticed in the various prepared nanocomposites.

3.3 Morphological investigation

SEM micrographs of $BaTiO_3/(ZnO)_x$ ceramics are showed in Fig. 4. Pure BTO sample (Fig. 4a) illustrated a morphology with homogeneous nanosized grains. The samples with ZnO doping showed an increase in the grains size in comparison to pure BTO product, but with lesser homogeneity. That is mostly due to the presence of secondary phase and the increment of sintering temperature with ZnO doping [28].

3.4 Optical investigation

Figure 5 presents the UV–Vis DRS of various synthesized $BaTiO_3/(ZnO)_x$ ceramics performed in the range of 200–800 nm. Tauc model was employed to deduce the optical band gap energy (E_g) according to the following expression [29]:

$$\alpha h\nu = \alpha\left(h\nu - E_g\right)^r \tag{2}$$

where $h\nu$ is the photon energy and α is a constant independent on photon energy. Since BTO has a direct band gap [30], the exponent r will take value of 1/2 and hence by plotting $(\alpha h\nu)^2$ as a function of $h\nu$, the E_g can be deduced. The E_g is deduced by extrapolating the linear portion to the low energies. The E_g values of $BaTiO_3/(ZnO)_x$ ceramics is deduced by converting the diffused reflectance values according to the Kubelka–Munk equation [31]:

$$F(R) = \alpha = \frac{(1-R)^2}{R} \tag{3}$$

Figure 6 presents plots of $(\alpha h\nu)^2$ against $h\nu$ where E_g values are deduced by extrapolating the linear portions. The deduced E_g values are listed in Table 2. The pristine BTO sample (x = 0 wt%) display E_g value of about 3.32 eV. The E_g value decreased with increasing the ZnO content. This reduction in the $BaTiO_3/(ZnO)$ ceramics could be ascribed to the increase in grains size and crystallinity [32]. This is supported by the XRD and SEM analyses. Another possible

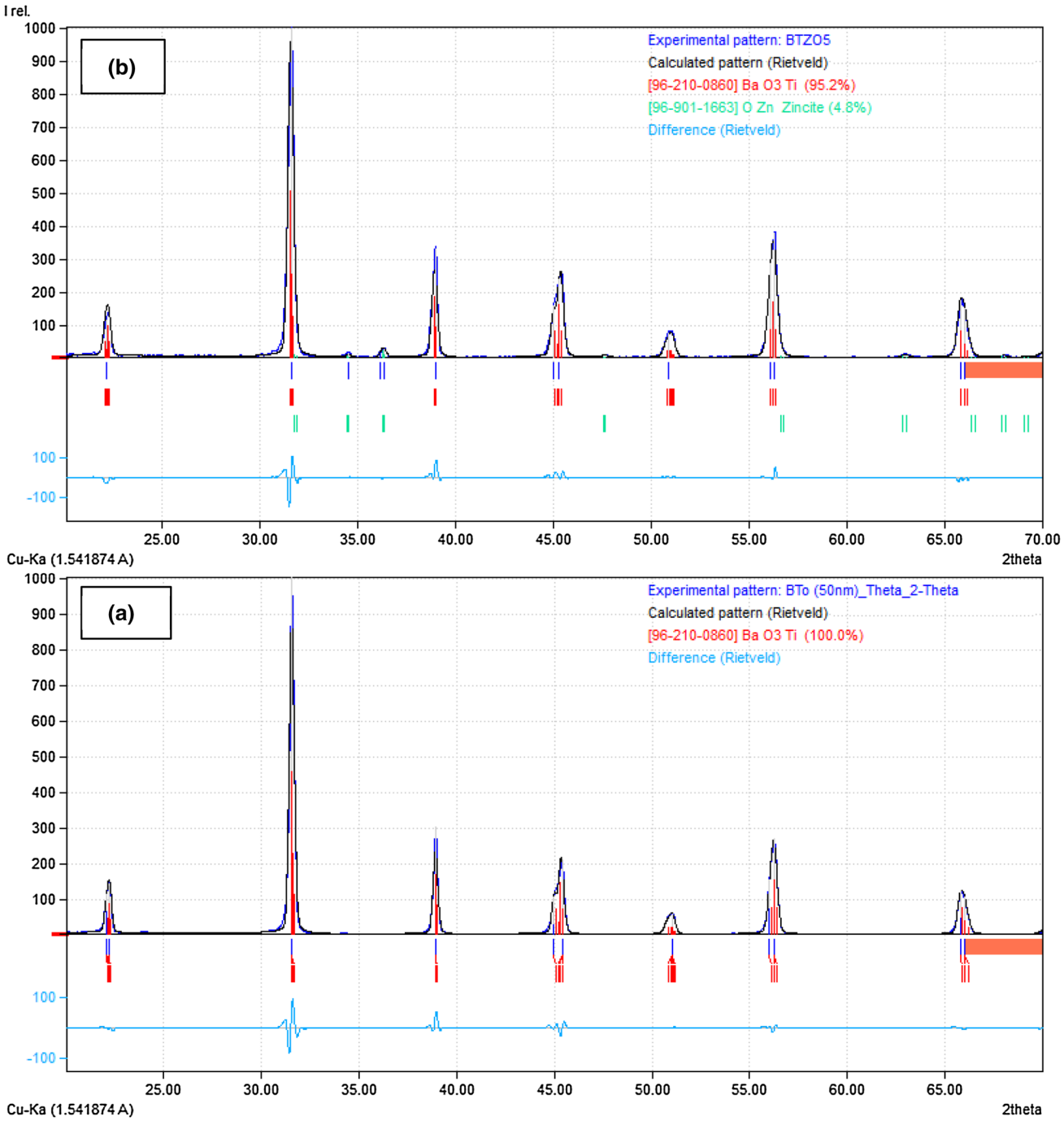

Fig. 2 Examples of XRD Rietveld refinements for **a** x = 0 and **b** 5 wt% nanocomposites

Table 1 Phase fractions and structural parameters of various $BaTiO_3/(ZnO)_x$ composites

x content (%)	Phase fractions (%)		Lattice parameters		c/a	D_{XRD} (nm)	R_B	χ^2
	$BaTiO_3$	Impurity	a = b (Å)	c (Å)				
0	100.0	0.0	3.9987	4.0283	1.0074	51.99	3.6	1.5
2	99.1	0.9	3.9975	4.0277	1.0075	65.28	2.8	0.9
5	95.2	4.8	3.9968	4.0272	1.0076	67.11	3.4	0.7
10	91.2	8.8	3.9966	4.0267	1.0075	69.36	3.1	1.2

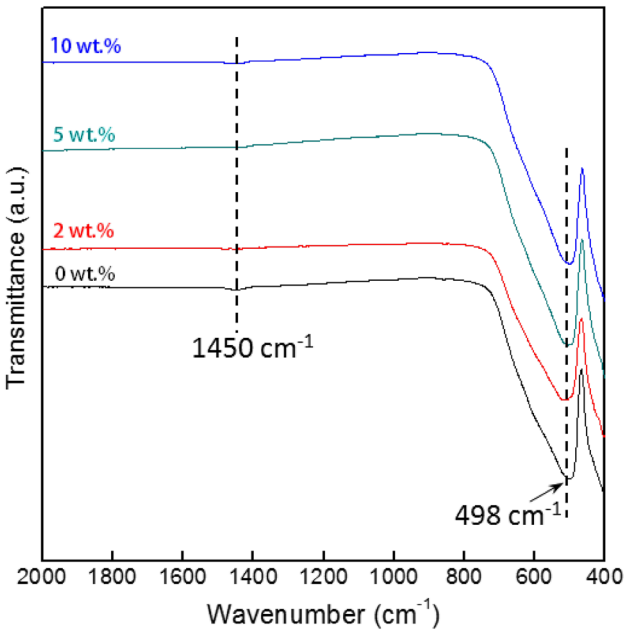

Fig. 3 FT-IR spectra of different prepared $BaTiO_3/(ZnO)_x$ nanocomposites where x = 0, 2, 5 and 10 wt%

reason for the change in E_g values is the presence of impurities in the $BaTiO_3/(ZnO)_x$ ceramics [33].

3.5 Dielectric analyses

The investigation of dielectric properties of materials is an essential tool to design passive devices for integrated circuits and microelectronic applications devices. The variation of dielectric constant (ε′) of $BaTiO_3/(ZnO)_x$ ceramics (x = 0, 2, 5 and 10 wt%) is compared in Fig. 7a. It is found that, for various compositions, the dielectric constant decreases quickly in the region of low-frequency and then became more or less constant at high frequency representing the dielectric dispersion. The high ε′ and the dielectric dispersion behavior at low frequency could be ascribed to the Maxwell–Wagner interfacial polarization consistent with Koop's phenomenological theory [34, 35]. Indeed, a dielectric compound having polycrystalline structure is supposed to be constituted of well conducting grains separated by highly resistive thin grain boundaries. The former is more efficient at lower frequencies whereas the grains are more efficient at high frequencies. Accordingly, the high ε′ at low frequency can be ascribed to the interfaces between the ferroelectric $BaTiO_3$ and the nano-phases ZnO that display considerably different permittivities and conductivities. When the composite is subjected to an electrical field, the

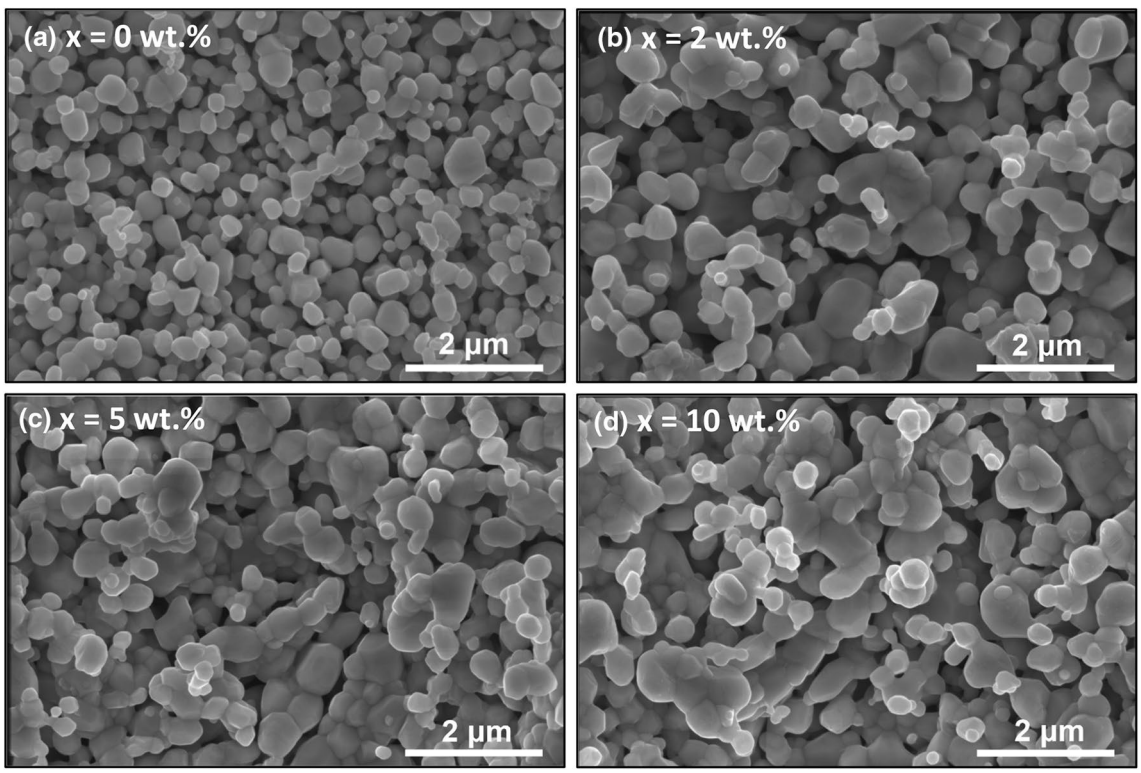

Fig. 4 SEM micrographs of the different synthesized $BaTiO_3/(ZnO)_x$ nanocomposites

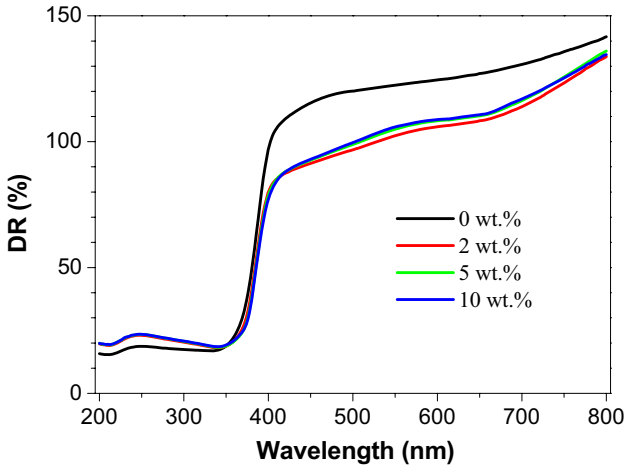

Fig. 5 DRS spectra of various prepared $BaTiO_3/(ZnO)_x$ nanocomposites

ZnO phase will provide space charges that accumulate at the interfaces of the two phases. Therefore, these interfaces provoke the additional polarization, i.e. interface polarization, that is inactive at higher frequencies because it is a typical slow polarization mechanism [36]. Consequently, it will lead to the dielectric dispersion at the lower frequencies. After the initial great values at low frequencies, the ε' becomes approximately constant at frequencies higher than 10 kHz. One should note that the dielectric permittivity for x = 2, 5 and 10 wt% samples shows a good stability in the frequency range 100 Hz–10 MHz, whereas pure BTO (x = 0 wt%) shows a strong dispersion. This result shows that the addition of ZnO nanoparticles improves the stability of the dielectric constant. This is encouraging for radio frequencies and microwaves applications. The dielectric constant also depended on the ZnO concentration, the greatest magnitude of $\varepsilon' = 1880$ was found for samples with x = 5 wt% of ZnO displaying a large and high density of granular microstructure and. The lowest magnitude of $\varepsilon' = 500$ was found for x = 10 wt% ceramic, which shows the large impurity compared with the other samples.

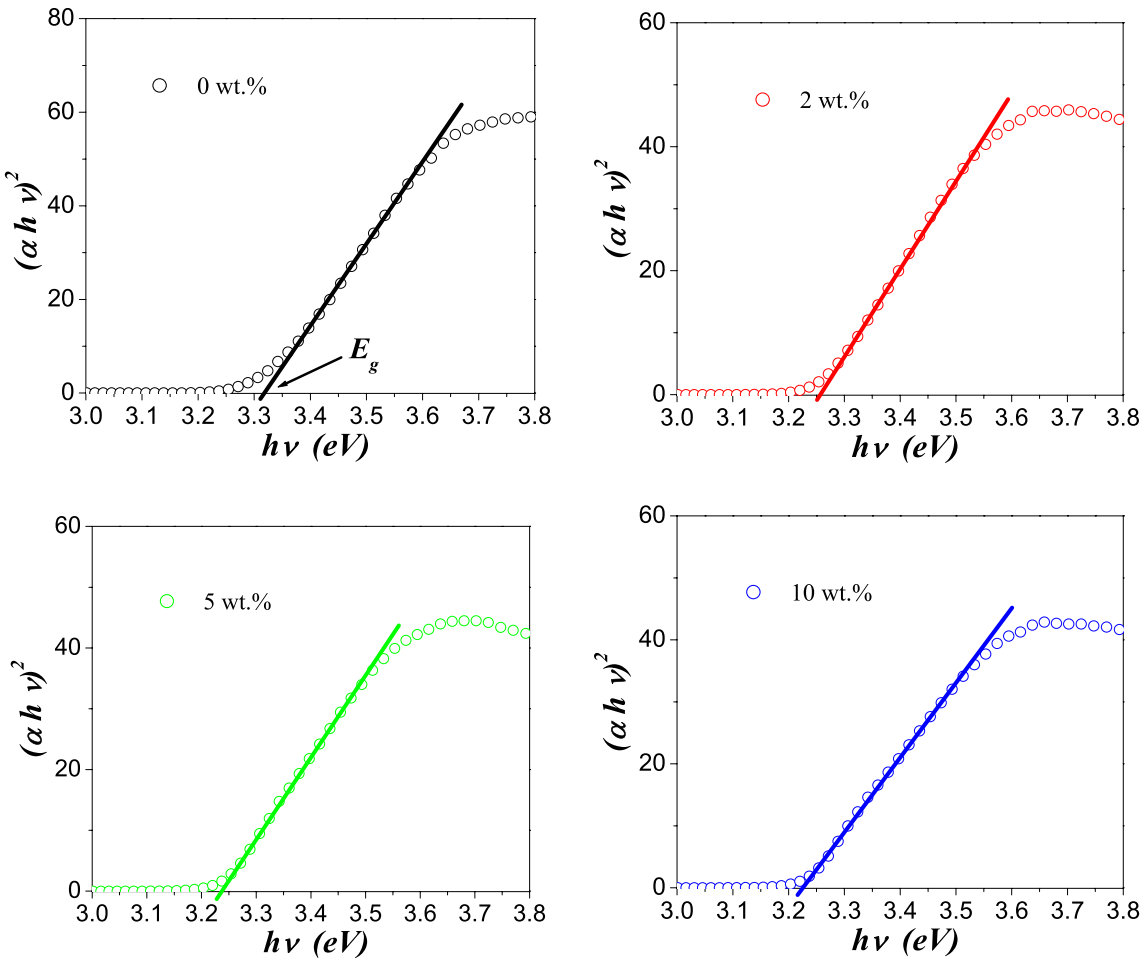

Fig. 6 Tauc plots of the different synthesized $BaTiO_3/(ZnO)_x$ nanocomposites

Table 2 E_g values deduced from Tauc plots for different synthesized $BaTiO_3/(ZnO)_x$ nanocomposites

x content (wt%)	E_g (eV)
0	3.32
2	3.26
5	3.23
10	3.22

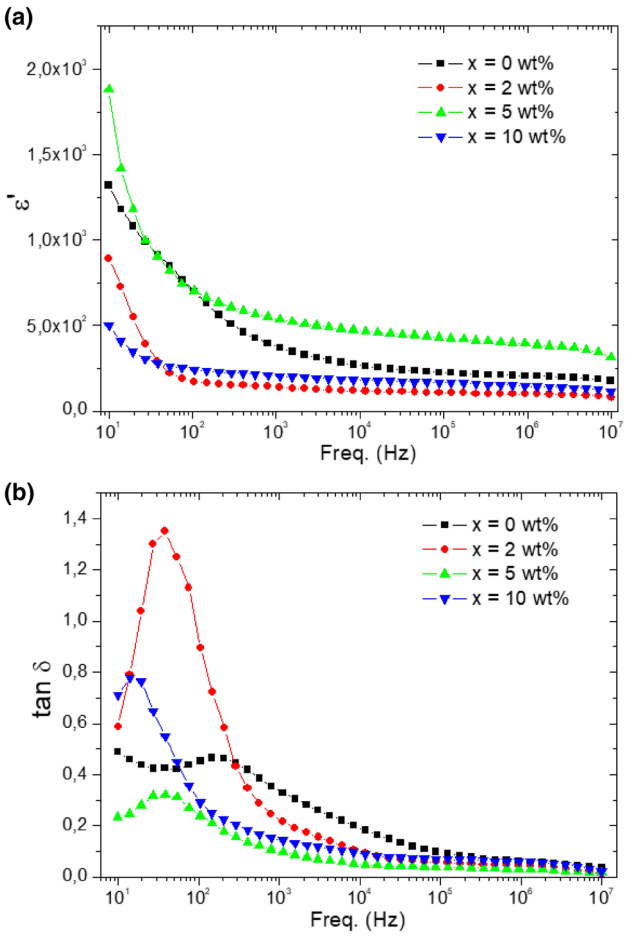

Fig. 7 Frequency dependence of **a** the dielectric constant ε′ and **b** the loss tangent (tan*)* of the various $BaTiO_3/(ZnO)_x$

The dispersion behavior observed in dielectric permittivity at low frequency is accompanied by a relaxation peak in loss tangent ($tg\delta = \varepsilon''/\varepsilon'$) as displayed in Fig. 1b. The dependence of dielectric loss on frequency indicates that the charge carriers hopping plays a significant role in their transport progressions since a loss peak is a basic characteristic of the charge carriers hopping transport [37]. After the peak observed at low frequency, the loss tangent (tgδ) for all samples decreases rapidly when the frequency increases. This behavior is also encouraging for microwave applications (high frequency). The dielectric loss (tanδ) is influenced by the ZnO concentration and is related to the sample microstructure. The lowest value of the dielectric loss ($tan\delta = 0.016$) was measured for x = 5 wt% ceramic. The x = 5 wt% ceramic exhibits the maximum permittivity and the lowest dielectric loss (tanδ) at room temperature, indicating that it is the most suitable concentration among the elaborated series. The high values and the good stability in a wide frequency range of dielectric permittivity combined with low dielectric loss (tgδ) make the $BaTiO_3/(ZnO)$ ceramics potential candidates for high frequency device applications, for decoupling capacitors, and for dynamic random-access memory. The dielectric, electric, mechanical properties over a large frequency and at various temperatures of the x = 5 wt% ceramic will be described in detail in a future investigation.

3.6 Electrical conductivity investigation

The ac conductivity (σ_{ac}) of various $BaTiO_3/(ZnO)_x$ ceramics is obtained using the following empirical formula:

$$\sigma_{ac} = \omega \cdot \varepsilon' \varepsilon_0 \tan(\delta) \quad (4)$$

where ε_0 is permittivity in vacuum and $\omega = 2\pi f$ is angular frequency. The results of σ_{ac} versus frequency were measured in the range $10\ Hz \leq F \leq 10^7 Hz$ at RT and presented in the Fig. 8. At low frequency, σ_{ac} is almost independent on frequency and this may be attributed to the dc conductivity of samples. When frequency is further increased, σ_{ac} is increased rapidly. The measured σ_{ac} versus frequency could be explained by the Jonscher's power law of the universal dielectric response (UDR) model [38]:

$$\sigma_{ac} = \sigma_{dc} + A\omega^n \quad (5)$$

where σ_{ac} is ac conductivity of the material, σ_{dc} is dc bulk conductivity, A is a thermally activated constant that

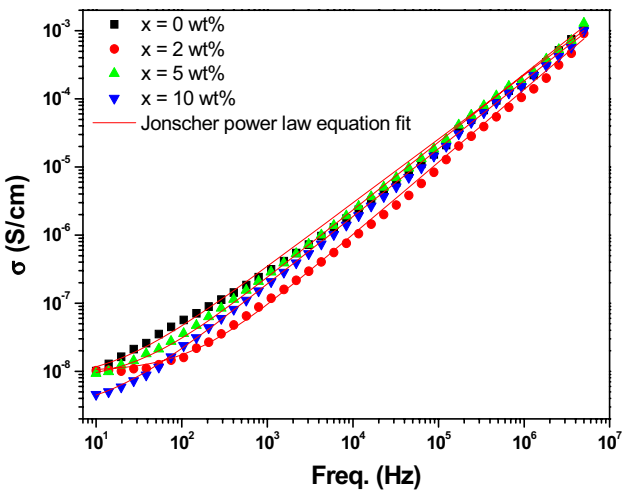

Fig. 8 AC conductivity (σ_{ac}) vesus frequency for $BaTiO3/(ZnO)_x$ ceramics at room temperature

Table 3 Dielectric constant (ε′), dielectric loss (tanδ) and fitting parameters using Eq. (5) for different $BaTiO_3/(ZnO)_x$ ceramics

x content (wt%)	Dielectric constant (ε)			Dissipation factor (tanδ)			σ_{dc} (Sm^{-1})	A	n
	10 Hz	45 kHz	10 MHz	10 Hz	45 kHz	10 MHz			
0	1320	236	176	0.48	0.12	0.03	7.12×10^{-9}	5.25×10^{-10}	0.9378
2	893	111	80	0.58	0.06	0.02	1.00×10^{-8}	5.46×10^{-11}	0.9982
5	1880	443	313	0.23	0.041	0.016	7.25×10^{-9}	2.37×10^{-10}	0.9978
10	500	171	114	0.71	0.073	0.021	2.55×10^{-9}	1.95×10^{-10}	0.9954

determines the polarizability strength, and n is a constant that determines the degree of interaction among the ions and lattice. The experimentally observed values of the samples using Eq. (5) were fitted and the obtained parameters are reported in Table 3. At lower frequency range, the experimental and theoretical values of pristine sample are not in good agreement, which is mostly owing to the existence of space charge polarization at the interface of sample-electrode. However, in all frequency range, the curves of x = 2, 5 and 10 wt% ceramics are well fitted. At higher frequency ($> 10^2$ Hz), the rise of ac conductivity with frequency may be accredited to electrons hopping between two different valence states [39]. It should be noted that the high frequency conductivity remains almost the same for all the ZnO concentrations, while a slight difference in conductivity is obtained at low frequency.

3.7 Electrical modulus analysis

For the composite structure, it is always better to know the effect of each phase (i.e., the dissociation between the bulk and the interface effect) and to highlight the effect of adding. The electric modulus (M^*) could give important details about the relaxation mechanism. This formalism has the advantage of suppressing the electrode effects, the grain-boundary conduction process and the undesirable influences of extrinsic relaxation [30]. The representation of the electric modulus to analyze dielectric properties is discussed in various reports [39–42]. Based on the complex permittivity $\varepsilon^* = \varepsilon' - j\varepsilon''$, M^* is expressed as follow:

$$M^* = M' + jM = \frac{\varepsilon'}{(\varepsilon'^2 + \varepsilon''^2)} + j\frac{\varepsilon''}{(\varepsilon'^2 + \varepsilon''^2)} \quad (6)$$

M′ and M″ are the real and imaginary parts of M^*, respectively.

Figure 9a presents variation of M′ versus frequency for $BaTiO_3/(ZnO)_x$ ceramics. At low frequency, the M' values are very low and approaches to zero for all compositions. The M′ value increased with increasing frequency. At high frequency region, M′ shows a continuous increase and dispersion. M' reached a maximum value corresponding to M_∞ (the asymptotic value of M′ at higher frequencies).

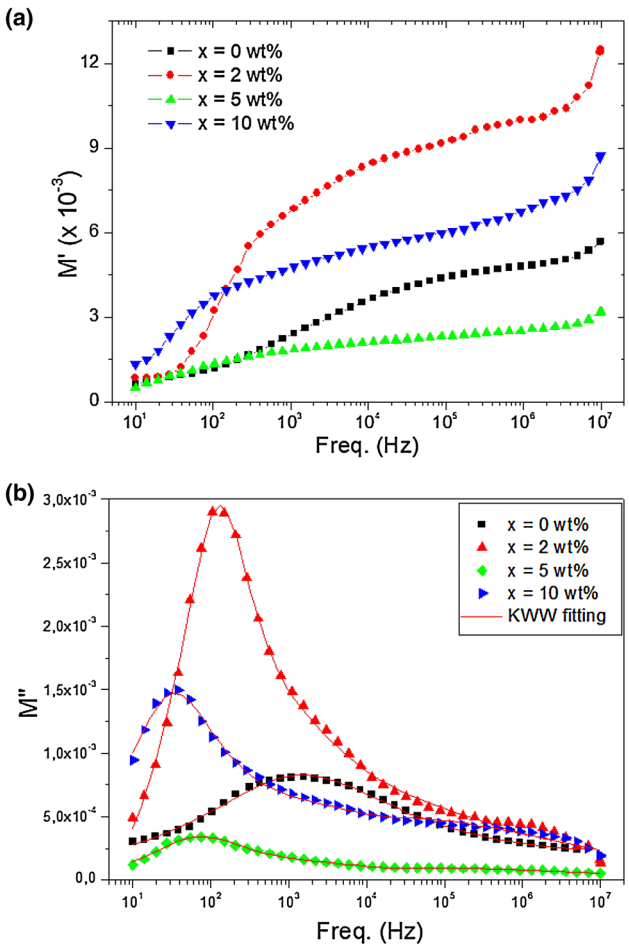

Fig. 9 Variation of **a** M′ and **b** M″ as a function of frequency for various $BaTiO_3/(ZnO)_x$ ceramics

The continuous dispersion as frequency increases could be accredited to the process of conduction because of the short-range mobility of charge carriers [43]. Besides, this effect could be associated to the non-existence of a restorative force that governs the charge carriers' mobility due to the induced electric field [43].

The evolution of M″ against frequency at RT is presented in Fig. 9b. The M″ plots exhibit clear characteristic peaks (at f_{max}) invented because of relaxation behavior and are in the center of the dispersion region of M′. The region

of frequency below f_{max} gives the extent to which charge carriers are mobile on long distances (Jump conduction process). At the frequencies above f_{max}, the carriers are confined to potential wells and hence are mobile on short distances [44]. The variation of the position peak (f_{max}) for the different samples may be attributed to the microstructure change and to the occurrence of a distribution of relaxation times.

M^* can be expressed as Fourier transform of a relaxation function ϕ(t) [45]:

$$M^* = M_\infty \left[1 - \int \left(\frac{d\phi}{dt}\right) e^{-iwt} dt\right] \quad (7)$$

where M^* is the electrical modulus and M_∞ represents the value of its real part at high frequencies. This equation used the Kohlrausch–Williams–Watts (KWW) function:

$$\phi(t) = e^{\left(\frac{t}{\pi}\right)^{\beta}}; \quad 0 < \beta \leq 1 \quad (8)$$

where β is an exponent indicating the Debye relaxation deviation (β = 1) and τ represents a characteristic relaxation time. The theoretical fits (solid lines) of the M″ experimental data are depicted in the Fig. 9b. Obviously, the experimental data are well fitted excepting in the region of high frequencies. The different fitted parameters (M_∞, β and τ) obtained by the KWW model for all compositions are reported in Table 4. The various fitting parameters are depending on the ZnO content. These values of β evidently imply the existence of non-ideal Debye-type relaxation phenomenon.

For the composite structure, it is always better to know the effect of each phase (i.e., the dissociation between the bulk and the interface effect. Figure 10 depicts M″ versus M′ for different $BaTiO_3/(ZnO)_x$ ceramics. It is clearly seen that the pure $BaTiO_3$ ceramics shows only one semi-circle, while two semi-circles are possibly traced for the x = 2, 5 and 10 wt% ceramics. This behavior suggests that the composite ceramics are composed of two phases which constituted of ZnO nanoparticles and $BaTiO_3$ elements. The semi-circle observed at lower frequencies is ascribed to the contributions of grain boundaries and the interfacial effect specified by the interface between the $BaTiO_3$ and the ZnO nanoparticles (interfacial properties), while the semi-circle occurred at higher frequency is associated to the grain (bulk properties).

Table 4 Adjustment parameters obtained by the model KWW for the $BaTiO_3/(ZnO)_x$ ceramics

x content (wt%)	M_∞	τ (s)	β
0	0.00259	0.00082	0.5325
2	0.01944	0.01315	0.8727
5	0.00057	0.01553	0.7386
10	0.00235	0.03446	0.7885

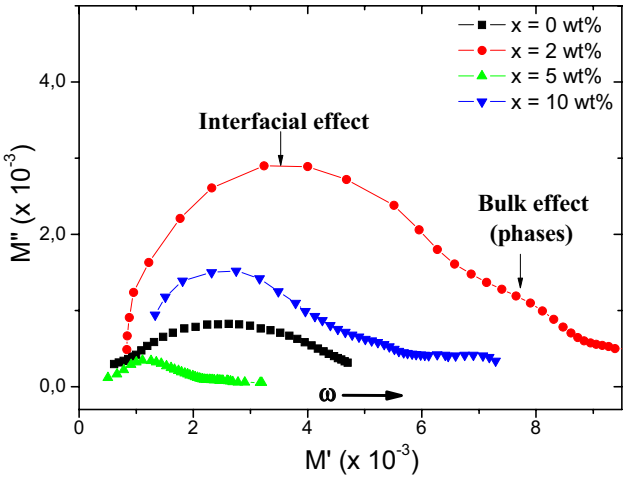

Fig. 10 M″ versus M′ of $BaTiO_3/(ZnO)_x$ (x = 0, 2, 5 and 10 wt%) ceramics

4 Conclusion

In this study, $BaTiO_3/(ZnO)_x$ ceramics (x = 0, 0.5, 1, 2 and 5 wt%) were successfully produced via solid state reaction. According to XRD analysis, pristine compound (i.e. x = 0 wt%) showed pure BTO phase with tetragonal structure. The tetragonality was maintained with ZnO additions. SEM observations showed an increase in grains size with increasing the ZnO concentration. Optical analyses revealed a reduction in E_g values, which is principally accredited to the increase of grains size. The investigation of electrical and dielectric properties indicated that the x = 5 wt% ceramic exhibits greatest dielectric constant and lowest tangent loss among various $BaTiO_3/(ZnO)_x$ ceramics. The obtained results are encouraging to use the optimal ceramic in radio frequencies and microwaves applications.

Acknowledgments The authors highly acknowledged the supports of the Institute for Research & Medical Consultations (Projects application No. 2017-IRMC-S-3, No. 2017-576-IRMC and No. 2018-IRMC-S-2) of Imam Abdulrahman Bin Faisal University (IAU—Saudi Arabia).

References

1. L. Xiaochi, W. Bian, Y. Li, H. Zhu, F. Zhenxiao, Q. Zhang, Influence of inverse spinel structured $CuGa_2O_4$ on microwave dielectric properties of normal spinel $ZnGa_2O_4$ ceramics. J. Am. Ceram. Soc. **101**, 1646–1654 (2018)
2. L. Xiaochi, W. Bian, C. Min, F. Zhenxiao, Q. Zhang, H. Zhu, Cation distribution of high-performance Mn-substituted

$ZnGa_2O_4$ microwave dielectric ceramics. Ceram. Int. **44**, 10028–10034 (2018)
3. C.D. Chandler, C. Roger, M.J. Hampdensmith, Chemical aspects of solution routes to perovskite-phase mixed-metal oxides from metal-organic precursors. Chem. Rev. **93**, 1205–1241 (1993)
4. M.A. Pena, J.L.G. Fierro, Chemical structures and performance of perovskite oxides. Chem. Rev. **101**, 1981–2017 (2001)
5. J. Harada, T. Pedersen, Z. Barnea, X-Ray and neutron diffraction study of tetragonal barium titanate. Acta Crystall. a-Crys. A **26**, 336 (1970)
6. F.I.H. Rhouma, A. Dhahri, J. Dhahri, H. Belmabrouk, M.A. Valente, Structural and dielectric properties of $Ba_{0.8}La_{0.133}Ti_{0.90}Sn_{0.1}O_3$. Solid State Commun. **152**, 1874–1879 (2012)
7. M.Z.C. Hu, G.A. Miller, E.A. Payzant, C.J. Rawn, Homogeneous (co)precipitation of inorganic salts for synthesis of monodispersed barium titanate particles. J. Mater. Sci. **35**, 2927–2936 (2000)
8. S. Dudley, T. Kalem, M. Akinc, Conversion of SiO_2 diatom frustules to $BaTiO_3$ and $SrTiO_3$. J. Am. Ceram. Soc. **89**, 2434–2439 (2006)
9. V. Paunovic, L. Zivkovic, Influence of Rare-earth additives (La, Sm and Dy) on the microstructure and dielectric properties of doped $BaTiO_3$ ceramics. Sci. Sinter. **42**, 69–79 (2010)
10. H.A. Moghaddam, M.R. Mohammadi, TiO_2-$BaTiO_3$ nanocomposite for electron capture in dye-sensitized solar cells. J. Am. Ceram. Soc. **100**, 2144–2153 (2017)
11. H.A. Moghaddam, M.R. Mohammadi, S.M.S. Reyhani, Improved photon to current conversion in nanostructured TiO_2 dye-sensitized solar cells by incorporating cubic $BaTiO_3$ particles deliting incident. Sol. Energy **132**, 1–14 (2016)
12. Y.M. Zhang, M.H. Cao, Z.H. Yao, Z.J. Wang, Z. Song, A. Ullah, H. Hao, H.X. Liu, Effects of silica coating on the microstructures and energy storage properties of $BaTiO_3$ ceramics. Mater. Res. Bull. **67**, 70–76 (2015)
13. W.H. Tzing, W.H. Tuan, H.L. Lin, The effect of microstructure on the electrical properties of NiO-doped $BaTiO_3$. Ceram. Int. **25**, 425–430 (1999)
14. T. Nagai, K. Iijima, H.J. Hwang, M. Sando, T. Sekino, K. Niihara, Effect of MgO doping on the phase transformations of $BaTiO_3$. J. Am. Ceram. Soc. **83**, 107–112 (2000)
15. Y. Sakabe, N. Wada, T. Hiramatsu, T. Tonogaki, Dielectric properties of fine-grained $BaTiO_3$ ceramics doped with CaO. Jpn. J. Appl. Phys. **41**, 6922–6925 (2002)
16. Y.H. Song, J.H. Hwang, Y.H. Han, Effects of Y_2O_3 on temperature stability of acceptor-doped $BaTiO_3$. Jpn. J. Appl. Phys. **44**, 1310–1313 (2005)
17. R. Saravanan, V.K. Gupta, E. Mosquera, F. Gracia, Preparation and characterization of V_2O_5/ZnO nanocomposite system for photocatalytic application. J. Mol. Liq. **198**, 409–412 (2014)
18. A.M. Al-syadi, V.K. Gupta, E. Mosquera, M.M. El-Desoky, M.S. Al-Assiri, Impedance spectroscopy of V_2O_5–Bi_2O_3–$BaTiO_3$ glass–ceramics. Solid State Sci. **26**, 72–82 (2014)
19. N. Zhang, L. Li, J. Chen, J. Yu, ZnO-doped $BaTiO_3$-$Na_{0.5}Bi_{0.5}TiO_3$-Nb_2O_5-based ceramics with temperature-stable high permittivity from − 55 °C to 375 °C. Mater. Lett. **138**, 228–230 (2015)
20. T. Wang, X. Wei, Q. Hu, L. Jin, Z. Xu, Y. Feng, Effects of $ZnNb_2O_6$ addition on $BaTiO_3$ ceramics for energy storage. Mater. Sci. Eng. B **178**, 1081–1086 (2013)
21. Y. Yan, C. Ning, Z. Jin, H. Qin, W. Luo, G. Liu, The dielectric properties and microstructure of $BaTiO_3$ ceramics with ZnO–Nb_2O_5 composite addition. J. Alloys. Compd. **646**, 748–752 (2015)
22. Q.K. Muhammad, M. Waqar, M.A. Rafiq, M.N. Rafiq, M. Usman, M.S. Anwar, Structural, dielectric, and impedance study of ZnO doped barium zirconium titanate (BZT) ceramics. J. Mater. Sci. **51**, 10048–10058 (2016)
23. Y. Iqbal, A. Jamal, The effect of Ta_2O_5- and ZnO-doping on the Curie temperature of $BaTiO_3$. J. Phys **371**, 012035 (2012)
24. A.C. Caballero, J.F. Fernández, C. Moure, P. Durán, Y.M. Chiang, Grain growth control and dopant distribution in ZnO-doped $BaTiO_3$. J. Am. Ceram. Soc. **81**, 939–944 (1998)
25. M. Atif, S. Ahmed, M. Nadeem, M.K. Ali, M. Idrees, R. Grossinger, R.S. Turtelli, Role of competing phases in the structural, magnetic and dielectric relaxation for $(1-x)CoFe_2O_4+(x)BaTiO_3$ composites. Ceram. Int. **42**, 14618–14626 (2016)
26. S. Lather, A. Gupta, J. Dalal, V. Verma, R. Tripathi, A. Ohlan, Effect of mechanical milling on structural, dielectric and magnetic properties of $BaTiO_3$-$Ni_{0.5}Co_{0.5}Fe_2O_4$ multiferroic nanocomposites. Ceram. Int. **43**, 3246–3251 (2016)
27. S. Kappadan, T.W. Gebreab, S. Thomas, N. Kalarikkal, Tetragonal $BaTiO_3$ nanoparticles: an efficient photocatalyst for the degradation of organic pollutants. Mater. Sci. Semicond. Process **51**, 42–47 (2016)
28. Y. Yan, L. Liu, C. Ning, Y. Yang, C.J. Xia, Y.T. Zou, S.Y. Liu, X.X. Wang, K.H. Liu, X.K. Liu, G. Liu, Improved electrical properties of SiO_2-added $BaTiO_3$ ceramics by microwave sintering. Mater. Lett. **165**, 135–138 (2016)
29. Y. Slimani, H. Gungunes, M. Nawaz, A. Manikandan, H.S. El Sayed, M.A. Almessiere, H. Sozeri, S.E. Shirsath, I. Ercan, A. Baykal, Magneto-optical and microstructural properties of spinel cubic copper ferrites with Li-Al co-substitution. Ceram. Int. **44**, 14242–14250 (2018)
30. P.G. Wang, C.M. Fan, Y.W. Wang, G.Y. Ding, P.H. Yuan, A dual chelating sol-gel synthesis of BaTiO3 nanoparticles with effective photocatalytic activity for removing humic acid from water. Mater. Res. Bull. **48**, 869–877 (2013)
31. Z.A. Garmaroudi, M.R. Mohammadi, Design of TiO_2 dye-sensitized solar cell photoanode electrodes with different microstructures and arrangement modes of the layers. J. Sol–Gel Sci. Techn. **76**, 666–678 (2015)
32. Y.C. Teh, A.A. Saif, Influence of annealing temperature on structural and optical properties of sol-gel derived $Ba_{0.9}Gd_{0.1}TiO_3$ thin films for optoelectronics. J. Alloys. Compd. **703**, 407–413 (2015)
33. L.V. Maneeshya, P.V. Thomas, K. Joy, Effects of site substitutions and concentration on the structural, optical and visible photoluminescence properties of Er doped $BaTiO_3$ thin films prepared by RF magnetron sputtering. Opt. Mater. **46**, 304–309 (2015)
34. T.G. Reddy, B.R. Kumar, T.S. Rao, J.A. Ahmad, Structural and dielectric properties of barium bismuth titanate ($BaBi_4Ti_4O_{15}$) ceramics. Int. J. Appl. Eng. Res. **6**, 571–580 (2011)
35. P. Jaita, A. Watcharapasorn, N. Kumar, D.P. Cann, S. Jiansirisomboon, Large electric field-induced strain and piezoelectric responses of lead-free $Bi_{0.5}(Na_{0.80}K_{0.20})_{0.5}TiO_3$-$Ba(Ti_{0.90}Sn0_{.10})O_3$ ceramics near morphotropic phase boundary. Electron. Mater. Lett. **11**, 828–835 (2011)
36. X.X. Dong, H.W. Chen, M. Wei, K.T. Wu, J.H. Zhang, Structure, dielectric and energy storage properties of $BaTiO_3$ ceramics doped with $YNbO_4$. J. Alloys. Compd. **744**, 721–727 (2018)
37. K. Kumari, A. Prasad, K. Prasad, Dielectric, Impedance/modulus and conductivity studies on $[Bi_{0.5}(Na_{1-x}K_x)_{0.5}]_{0.94}Ba_{0.06}TiO_3$,$[0.16 \le x \le 0.20]$ leadfree ceramics. Am. J. Mater. Sci. **6**, 1–8 (2016)
38. A.K. Jonscher, The 'universal'dielectric response. Nature **267**, 673 (1977)
39. L. Singh, U.S. Rai, K. Mandal, B.C. Sin, S.I. Lee, Y. Lee, Dielectric, AC-impedance, modulus studies on $0.5BaTiO_3 \cdot 0.5CaCu_3Ti_4O_{12}$ nano-composite ceramic synthesized by one-pot, glycine-assisted nitrate-gel route. Ceram. Int. **40**, 10073–10083 (2014)
40. A. Rouahi, A. Kahouli, F. Challali, M.-P. Besland, C. Vallée, B. Yangui, S. Salimy, A. Goullet, A. Sylvestre, Impedance and

electric modulus study of amorphous TiTaO thin films: highlight of the interphase effect. J. Phys. D **46**, 065308 (2013)
41. A. Selmi, O. Khaldi, M. Mascot, F. Jomni, J. Carru, Dielectric relaxations in $Ba_{0.85}Sr_{0.15}TiO_3$ thin films deposited on Pt/Ti/SiO_2/Si substrates by sol–gel method. J. Mater. Sci. **27**, 11299–11307 (2016)
42. M. Sahu, S.K. Pradhan, S. Hajra, B.K. Panigrahi, R. Choudhary, Studies of structural, electrical, and excitation performance of electronic material: europium substituted $0.9(Bi_{0.5}Na_{0.5}TiO_3)$–$0.1(PbZr_{0.48}Ti_{0.52}O_3)$. Appl. Phys. A **125**, 183 (2019)
43. C. Rayssi, S.E. Kossi, J. Dhahri, K. Khirouni, Frequency and temperature-dependence of dielectric permittivity and electric modulus studies of the solid solution $Ca_{0.85}Er_{0.1}Ti_{1-x}Co_{4x/3}O_3$ ($0 \le x \le 0.1$). RSC Adv. **8**, 17139–17150 (2018)
44. R. Schmidt, S. Pandey, P. Fiorenza, D.C. Sinclair, Non-stoichiometry in "$CaCu_3Ti_4O_{12}$" (CCTO) ceramics. RSC Adv. **3**, 14580–14589 (2013)
45. A. Rouahi, A. Kahouli, A. Sylvestre, E. Defay, B. Yangui, Impedance spectroscopic and dielectric analysis of $Ba_{0.7}Sr_{0.3}TiO_3$ thin films. J. Alloys. Compd. **529**, 84–88 (2012)